BULLETIN OF THE POLISH ACADEMY OF SCIENCES
TECHNICAL SCIENCES,
DOI:10.24425/bpasts.2025.153828

Strategic Optimal Control of Multi-Camera Trajectories for UAV Capture Using Entropy and Coverage Approaches

Khishigjargal GONCHIGSUMLAA[1], Young-il KIM[2], Kun Min YEO[3], Seong Hee PARK[3] and Yong Tae LEE[3],*

[1] University of Science and Technology (UST), 217, Gajeong-ro, Daejeon, 34113, South Korea
[2] Yiseotec Co.Ltd, 18, Saeromnam-ro, Sejong-si, 30126, South Korea
[3] Electronics and Telecommunications Research Institute (ETRI), 218, Gajeong-ro, Daejeon, 34129, South Korea

Abstract. The widespread use of unmanned aerial vehicles (UAVs) has heightened the demand for effective UAV monitoring, particularly in protected areas. Current learning-based detection systems depend heavily on camera sensors' ability to capture UAVs in surveillance areas; however, advanced camera control methods remain limited. This paper proposes determining multi-camera trajectories that maximize UAV capture probability, ensuring UAVs remain within the camera's field of view for further analysis, such as detection methods from camera-shot images. For this purpose, stochastic modelling is considered in the control framework for optimizing surveillance camera trajectories to enhance the probability of capturing UAVs. Key control parameters are derived through classical probability evaluations of the model with maximizing the entropy and covering trajectory-based strategies are applied. The reliability of stochastic system modeling is empirically validated through comprehensive computational experiments. These findings demonstrate the model's potential to enhance UAV capture rates through optimized camera trajectories and coverage efficiency, paving the way for future advancements in real-environment applications.

Key words: optimal control; multi-camera trajectory; unmanned aerial vehicle; entropy maximization; surveillance area

1. INTRODUCTION

A UAV, or unmanned aerial vehicle, is an aircraft operated either autonomously or through remote control, without an onboard pilot [1, 2]. Although UAVs are primarily employed in disaster response, medical rescue operations, and package delivery due to unstable geopolitical conditions [3], they are increasingly developed for applications across scientific fields and various industrial sectors [2, 3]. Despite these advantages, due to their mobility and ease of use, UAVs can be misused for unauthorized surveillance, smuggling, or targeted attacks, raising concerns about the security of sensitive and restricted areas [4, 5]. Consequently, developing effective UAV detection systems has become a priority in modern surveillance and security strategies [6, 7]. This recent need has led to extensive research efforts to develop solutions to address these security challenges. To address these security challenges, considerable research has focused on UAV detection and tracking, demonstrating the effectiveness of computer vision and AI-based methods using cameras, radar, RF signals, infrared, and acoustic sensors, depending on the UAV's location, speed, and purpose [8–10]. Camera-based methods are particularly popular due to their flexibility, accuracy, and efficiency compared to radar, acoustic, and RF-based techniques. To ensure optimal performance of the AI algorithm, high-quality images of the UAV are essential, [11], which means it can only identify the UAV after it appears on the camera screen. Without proper camera capture, AI detection is ineffective. Thus, the camera must first capture the UAV with optimal efficiency. In other words, extensive research addresses AI-based recognition of UAVs, but there is comparatively little on optimizing the camera's role in detecting UAVs as they enter the field of view (FOV). Overlapping FOV between adjacent cameras is essential to ensure continuous coverage in the surveillance multi-camera system.

Existing achievements have focused on creating effective camera surveillance systems that reduce blind spots and cover large areas, ensuring continuous monitoring of UAVs. Multi-camera systems have been studied for numerous applications using different layouts, configurations, and algorithms, and their importance is obvious [12, 13]. Pan-tilt-zoom (PTZ) cameras are essential for dynamic surveillance applications, providing flexible control over camera orientation and zoom to capture detailed images across wide areas. The PTZ and intelligent camera technologies have significantly advanced the field of camera control and coordination in surveillance systems [12, 14]. While using multiple cameras may pose economic challenges, the feasibility of employing spiral rotating cameras for UAV detection and monitoring is explored [15]. The previously referenced article emphasizes the importance of high-quality UAV images and proposes a method for structuring a UAV surveillance area to capture these images effectively. It also explores ways to reduce the number of cameras in image sensing while maintaining necessary image quality, thereby advancing UAV detection technology through optimized camera usage. [11].

This study presents a comprehensive model integrating multi-camera systems and UAV motion dynamics within a single surveillance area. Specifically, the surveillance area is subdivided into adjacent subareas, each monitored by an individual camera, and the motion paths of multiple UAVs are modeled in the entire surveillance area. During the UAVs' dwell time within the surveillance area, the probabilities for each

*e-mail: ytlee@etri.re.kr

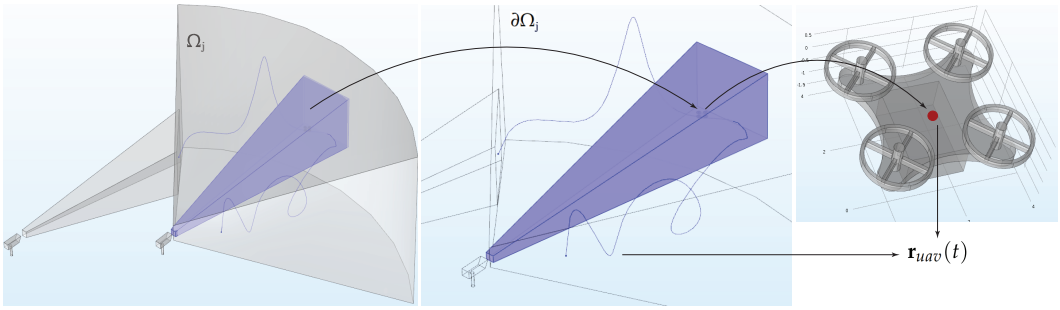

Fig. 1. The environment of surveillance area, Left: Ω_j is jth surveillance area, Center: camera's field of view and $\partial\Omega_j$ is the boundary of surveillance area, Right: $\mathbf{r}_{uav}(t)$ is the centroid of UAV/multimotor.

camera are considered, while maintaining the unique coverage trajectories of the cameras. For this purpose, UAV motion is modeled using Stochastic Differential Equations (SDE), with relevant models for UAVs detailed in [16, 17]. When modeling camera movements through three distinct trajectories, each must ensure coverage of all points within the subarea. A general algorithm for coverage path planning and autonomous device coverage is available [18, 19]. To model the complex dynamics of multiple UAVs, we employ SDE, while the Hamilton-Jacobi-Bellman (HJB) equation maximizes differential entropy, allowing for optimal camera trajectories under uncertainty. To assess the multi-camera capturing probabilities for multiple UAVs during their coverage of the surveillance area, the Fokker-Planck equation (FPE) is employed. For models based on the FPE, we refer to the review in [20, 21], which includes numerical computations [22]. A predefined camera trajectory is also introduced and designed to ensure comprehensive area coverage and increase UAV capture probability.

The contributions of this study to the academic literature are outlined below:

- *Integrated modeling for UAVs and cameras dynamics*: classic SDE is used for modeling the UAV dynamics to integrate the model with FPE to gain the joint PDF in representing the spatio-temporal distributions of UAV and camera trajectories, capturing both deterministic and stochastic behaviors.
- *Empiric evaluation of the integrated model*: for the reliability of the model, which has been designed especially for the considering problem, we introduced an indicator function to evaluate the capturing probability of the camera. The empiric evaluation expressed the models' reasonable features.
- *Entropy maximizing based optimal control approach*: the application of differential entropy is introduced to the classic differential equation for optimal control, enabling the determination of optimal camera paths that effectively improve detection uncertainty.
- *Cover trajectory maximizing based optimal control approach*: a predefined trajectory maximizes area coverage and UAV capture probability, enhancing the system's effectiveness in wide-area monitoring and supporting improved real-time responses.

The rest of this paper is organized into four sections. In Section 1, we discuss the research background, motivation, and the importance of multi-camera systems for monitoring UAVs. Section 2 details the methodological framework while section 3 describes the research computational results and discussion. Finally, Section 4 synthesizes the research findings and offers conclusive insights.

2. METHODOLOGY

2.1. Stochastic modelling of UAV motion and surveillance camera's frustum

In the context of UAV attacks, it is crucial to recognize that such events are inherently unpredictable. Furthermore, it is important to highlight that the overall trajectory of UAV, particularly a multi-motor UAV, is characterized by significant uncertainty from its capability to navigate in all directions, the variability in reaching its final destination, and the unpredictability of its stopping time. The stochastic modelling is mainly used to investigate such random events [16]. Let N represent the number of UAVs in the surveillance area, and let the three-dimensional coordinates of their paths be:

$$\mathbf{r}_{uav_i}(t) = (x_{uav_i}(t), y_{uav_i}(t), z_{uav_i}(t))^\top, \quad i = \overline{1,N}. \tag{1}$$

Paths are considered as the coordinates of UAV's centroids, as depicted in Fig. 1. Then each $\mathbf{r}_{uav_i}(t)$ during UAV's existence time t in the surveillance area is governed by a SDE [17] through components as:

$$\begin{aligned} dx_{uav_i}(t) &= \mu_x(\mathbf{r}_{uav_i}(t),t)dt + \delta_x(\mathbf{r}_{uav_i}(t),t)dw_x(t) \\ dy_{uav_i}(t) &= \mu_y(\mathbf{r}_{uav_i}(t),t)dt + \delta_y(\mathbf{r}_{uav_i}(t),t)dw_y(t) \\ dz_{uav_i}(t) &= \mu_z(\mathbf{r}_{uav_i}(t),t)dt + \delta_z(\mathbf{r}_{uav_i}(t),t)dw_z(t), \end{aligned} \tag{2}$$

where $\Omega = \bigcup_{j=1}^{M} \Omega_j$ is surveillance area which consists of M subareas, each monitored by a surveillance camera covering the j^{th} area. Terms $\delta_x(\mathbf{r}_{uav_i}(t),t)$, $\delta_y(\mathbf{r}_{uav_i}(t),t)$, and $\delta_z(\mathbf{r}_{uav_i}(t),t)$ denote the diffusion components, while $\mu_x(\mathbf{r}_{uav_i}(t),t)$, $\mu_y(\mathbf{r}_{uav_i}(t),t)$, and $\mu_z(\mathbf{r}_{uav_i}(t),t)$ represent the drift components for the x, y, and z components of the process, respectively. Moreover, $w_x(t)$,$w_y(t)$, and $w_z(t)$ describe the changes in three separate (independent) Wiener processes for each component, introducing independent sources of randomness into each of the three components. Additionally, since the UAV's motion must remain within the domain Ω, any outward motion is not interesting (irrelevant). Thus, the corresponding

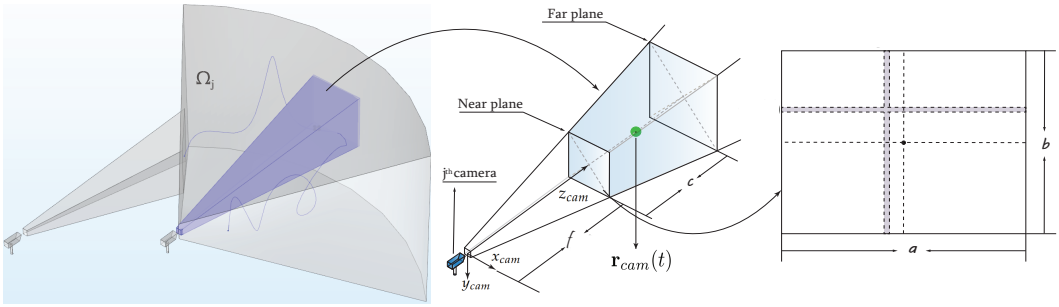

Fig. 2. The environment of the surveillance area, Left: Ω_j is jth surveillance area, Center: The centroid of camera's frustum and parameters of the camera, Right: the image sensing plane of the camera.

boundary condition for bounce back is as follows:

$$\mathbf{r}_{uav_i}(t) = \begin{cases} 2\mathbf{r}_{\max} - \mathbf{r}_{uav_i}(t), & \text{if } \mathbf{r}_{uav_i}(t) > \mathbf{r}_{\max}, \\ 2\mathbf{r}_{\min} - \mathbf{r}_{uav_i}(t), & \text{if } \mathbf{r}_{uav_i}(t) < \mathbf{r}_{\min}. \end{cases}$$

Deterministic components vary by UAV type; for instance, fixed-wing drones exhibit a drifting process, while multi-motor drones are preferred without drift.

The surveillance camera is assumed to be a PTZ model in this research. From a camera perspective, each camera's FOV can be conceptualized as a truncated pyramid in the horizontal direction, as shown in Fig. 2. In this framework, the world coordinate of the centroid of this truncated pyramidal shape is denoted as:

$$\mathbf{r}_{cam_j}(t) = (x_{cam_j}(t), y_{cam_j}(t), z_{cam_j}(t))^\top. \tag{3}$$

While the camera rotates dynamically to monitor the surveillance area, the centroid coordinates indicate the camera's motion paths in real three-dimensional space. The truncated pyramid defines the camera's potential FOV, commonly referred to as the camera's frustum [23]. When a UAV enters the frustum, the camera captures its image on the imaging plane.

2.2. Comprehensive modelling of multi-camera tracking probability for multiple UAVs

We consider two types of trajectories for surveillance cameras—namely, the optimal trajectory and the coverage trajectory. In the optimal trajectory, cameras follow the trajectories to increase the number of UAV captures by maximizing the system entropy. In the cover trajectory, initially, the trajectory is defined to cover the entire area and the camera must follow only that predetermined trajectory to conserve energy. The following notations are used in evaluating the probability of capturing multiple UAVs by multiple cameras in a surveillance area,

$$\mathbf{r}_{uavs}(t) = (\mathbf{r}_{uav_1}(t), \mathbf{r}_{uav_2}(t), \ldots, \mathbf{r}_{uav_N}(t))$$
$$\mathbf{r}_{cams}(t) = (\mathbf{r}_{cam_1}(t), \mathbf{r}_{cam_2}(t), \ldots, \mathbf{r}_{cam_M}(t)),$$

where each $\mathbf{r}_{uav_i}(t)$ is defined in entire Ω and each $\mathbf{r}_{cam_j}(t)$ monitors Ω_j, which is the j^{th} subarea of Ω. The technical parameters of all surveillance cameras are assumed to be identical. For simplicity in notation, we define $\mathbf{r}_{uavs}(t) = r_{uavs}$, $\mathbf{r}_{cams}(t) = r_{cams}$, and $(\mathbf{r},t) = (r_{uavs}, r_{cams}, t)$. Subsequently, the joint PDF $p(\mathbf{r},t)$ describes the likelihood of cameras and UAVs, and satisfies the following FPE:

$$\begin{aligned} \frac{\partial p(\mathbf{r},t)}{\partial t} = &- \sum_{i=1}^{N} \nabla_{uav_i} \cdot \Big(\mathbf{b}_{uav_i}(\mathbf{r}_{uav_i},t) p(\mathbf{r},t) \Big) \\ &- \sum_{j=1}^{M} \nabla_{cam_j} \cdot \Big(\mathbf{b}_{cam_j}(\mathbf{r}_{cam_j},t) p(\mathbf{r},t) \Big) \\ &+ \frac{1}{2} \sum_{i=1}^{N} \nabla_{uav_i} \cdot \Big(D_{uav_i}(\mathbf{r}_{uav_i},t) \nabla_{uav_i} p(\mathbf{r},t) \Big). \end{aligned} \tag{4}$$

Recall that N represents the number of UAVs, and M denotes the number of cameras. In Eq. (2), the drift and diffusion terms take the following form:

$$\mathbf{b}_{uav_i}(\mathbf{r}_{uav_i},t) = \begin{bmatrix} \mu_x(r_{uav_i},t) \\ \mu_y(r_{uav_i},t) \\ \mu_z(r_{uav_i},t) \end{bmatrix},$$

$$D_{uav_i}(\mathbf{r}_{uav_i},t) = \begin{bmatrix} \sigma_x^2(\mathbf{r}_{uav_i},t) & 0 & 0 \\ 0 & \sigma_y^2(\mathbf{r}_{uav_i},t) & 0 \\ 0 & 0 & \sigma_z^2(\mathbf{r}_{uav_i},t) \end{bmatrix}.$$

The $\mathbf{b}_{cam_j}(\mathbf{r}_{cam_j},t)$ is the drift coefficient for the camera, determined by the trajectory of the camera. Since the dynamic motion of both UAV and camera are confined within the observing area, a no-flux boundary condition is enforced to ensure that the total probability remains conserved:

$$\frac{\partial p(\mathbf{r},t)}{\partial \mathbf{n}} = 0 \quad \text{on } \partial\Omega.$$

This Neumann boundary condition maintains stable and unique conditions for numerical solving with natural enforcing normalization of the probability distribution over the domain, [24, 25]:

$$\int_\Omega p(\mathbf{r},t) d\mathbf{r} = 1.$$

Moreover, for the joint distribution, we have the following initial conditions:

$$p(\mathbf{r},0) = p(\mathbf{r}_{uavs}(0)) p(\mathbf{r}_{cams}(0)). \tag{5}$$

Here, $\mathbf{r}_{uavs}(0)$ and $\mathbf{r}_{cams}(0)$ are the initial positions of each UAV and camera, respectively. Let t be the random time during

the UAV and camera actions, and define the following times:

$$\tau_i = \inf\{t > 0 |\ \|\mathbf{r}_{uav_i}(t) - \partial\Omega\|_2 \le d_\varepsilon\},$$

$$\tau_j = \inf\{t > 0 \left|\begin{array}{l} |x_{uav_i}(t) - x_{cam_j}(t)| < a \\ |y_{uav_i}(t) - y_{cam_j}(t)| < b \\ |z_{uav_i}(t) - z_{cam_j}(t)| < c\}, \end{array}\right.$$

d_ε represents a distance threshold of $\partial\Omega$, the boundary of the monitoring area Ω, and the parameters a and b refer to the dimensions of the camera's projection plane, while c represents the distance between the near and far planes of the camera, as illustrated in Fig. 2. By assuming that the starting positions of UAV and camera must be independent, the expression (5) is derived using the chain rule. For evaluating the camera's UAV capturing probability, the indicator function is used as:

$$I_{i,j}(\mathbf{r},t) = \begin{cases} 1, & \tau_i(\mathbf{r},t) < \tau_j(\mathbf{r},t) \\ 0, & \text{otherwise}, \end{cases}$$

then the capture probability of the j^{th} camera at time t before the UAV reaches the boundary of the surveillance area can be expressed:

$$P_j(t) = \int_{\Omega_j} I_{i,j}(\mathbf{r},t)p(\mathbf{r},t)d\mathbf{r}. \tag{6}$$

The integral represents the evolution of time in which the camera captures the UAV, essentially calculating the total probability of the detection event occurring within the specified region. To compute the capture probability $P_j(t)$, the FPE must be solved. Despite significant advancements in analytical and numerical methods for solving FPE, achieving solutions within specific predefined regions remains a persistent challenge.

3. COMPUTATION RESULTS AND DISCUSSION

3.1. A UAV-driven analysis for model investigation

For analysis of the reliability of the model, we fix the camera trajectory as covering and change the number of UAVs. When the number of UAVs increases the number of capture probability must be increased if the model is authentic. Hence, to streamline the computation of the capture probability and address FPE, the surveillance area is transformed into a two-dimensional domain, as shown in Fig. 3, left. The chosen projection plane is carefully oriented to coincide with the camera's image plane, facilitating subsequent computations in the next section. The projection plane of Ω_i is denoted as $\overline{\Omega}_i$, and the dimensions of the projection plane are specified as $2R_{\max} \times 2R_{\max}$, with $R_{\max}$ denoting the distance of the camera's far field. The method of projecting the surveillance area gives us significant advantages in numerical computation for solving the FPE regarding its initial conditions. The camera's far-field covers approximately 400 meters and was taken from an average of PTZ cameras. Consequently, the total surveillance area is 400 meters by 800 meters, consisting of two adjacent areas, each measuring 400 meters by 400 meters for $\overline{\Omega}_1$ and $\overline{\Omega}_2$ in Fig. 3, left.

Note that with this projection plane, only the multi-motor UAV is focused, because of its complicated feature of flight ability compared to fixed wing. For this purpose, we suggested the following specified functions for drone's drift and diffusion:

$$\begin{cases} \mu_x(\mathbf{r}_{uav_i}(t),t) = x_{uav_i}(t)|\tan(t)| + y_{uav_i}(t) \\ \sigma_x(\mathbf{r}_{uav_i}(t),t) = y_{uav_i}(t)|\cot(t)| \end{cases}$$

$$\begin{cases} \mu_y(\mathbf{r}_{uav_i}(t),t) = y_{uav_i}(t)|\tan(t)| + x_{uav_i}(t) \\ \sigma_y(\mathbf{r}_{uav_i}(t),t) = x_{uav_i}(t)|\cot(t)|. \end{cases}$$

These functions are employed to present the drone's unique flying capabilities. Specifically, the drone exhibits a flight pattern characterized by straight-line segments followed by circular trajectories. It can pause during a straight-line flight and subsequently resume in a circular path. The random motion emulates the drone's observed phenomena are depicted in Fig. 3, right. The Zigzag type trajectory of the camera, encompassing various trajectory types considered in the subsequent section 3.3 and Fig. 7, left. Utilizing the projection plane as

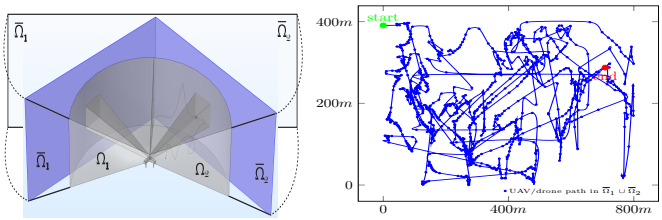

Fig. 3. The projection planes for surveillance areas, Left: $\overline{\Omega}_j$ is the projection plane of Ω_j, Right: 2D path of the UAV/multimotor in $\overline{\Omega}_1 \cup \overline{\Omega}_2$.

a simplified domain, the Finite Difference Method (FDM) is applied to solve the FPE, which characterizes the initial conditions expressed in Eq. (5). Since all UAVs initially start from the left side of the surveillance area, the initial distribution of UAVs has a long peak along the left part of the domain Fig. 4, left. Subsequently, the initial distribution of the camera has two peaks for the starting positions of the two cameras Fig. 4, center. Using these representations of initial distributions for UAVs and cameras, the joint initial distribution is computed using Eq. (5) and shown in Fig. 4, right.

The natural discretization is used to grid the domain into finite uniform node points, and the centered difference method is applied in FDM for improving the truncation errors. The grid size of dividing the domain is $\Delta y = 0.1$ and $\Delta x = 2\Delta y$ for the $400m \times 800m$ dimensional domain, and the time is discretized to evaluate the system for each second. The time evolutionary numerical solutions of the FPE are depicted in Fig. 5, with corresponding selected times, and a pseudo-code description of the numerical solving algorithm is expressed in Algorithm 1. In each iteration, UAVs and cameras adjust their positions according to their respective motion rules. For instance, all UAVs move in random directions determined by a stochastic process with specific drift and diffusion laws. Although the paths of these UAVs exhibit significant diversity due to their random nature, they all originate from the left side of the three-dimensional surveillance area within the projection domain. Consequently, the time-evolutionary numerical solutions of the FPE encapsulate all phenomena related to the

Algorithm 1 The algorithm of solving Fokker-Planck Equation (4) with varying UAV

Initialize parameters:
Define spatial grid: Δx and Δy and give time step: Δt
Define number cameras M and give initial number of UAVs N
Set initial probability distribution $p(\mathbf{r}, t=0)$
Initialize drift coefficients μ_x, μ_y for UAVs and cameras
Initialize diffusion coefficients σ_x, σ_y for UAVs
Start N=2
for each time step $t=0$ to T_{max} with step size Δt **do**
  for each UAV $i=1$ to N **do**
    for each grid point (x,y) **do**
      $b_{uav} \leftarrow [\mu_x(x,y,t)\ \mu_y(x,y,t)]^\top$
      // Update drift term: $\nabla \cdot (\mathbf{b}_{uav} p)$
      drift_uav_x $\leftarrow \frac{(p[x+1]-p[x-1])}{2\Delta x}\mu_x + \frac{(\mu_x[x+1]-\mu_x[x-1])}{2\Delta x}p[x]$
      drift_uav_y $\leftarrow \frac{(p[y+1]-p[y-1])}{2\Delta y}\mu_y + \frac{(\mu_y[y+1]-\mu_y[y-1])}{2\Delta y}p[y]$
    end for
    for each grid point (x,y) **do**
      $D_{uav} \leftarrow \begin{bmatrix}\sigma_x^2 & 0\\ 0 & \sigma_y^2\end{bmatrix}$
      // Update diffusion term: $\nabla \cdot (D_{uav} \nabla p)$
      diff_uav_x $\leftarrow \frac{\sigma^2[x+1]-\sigma^2[x-1]}{\Delta x^2}\frac{(p[x+1]-p[x-1])}{2\Delta x}$
        $+\sigma^2[x]\frac{p[x+1]-2p[x]+p[x-1]}{\Delta x^2}$
      diff_uav_y $\leftarrow \frac{\sigma^2[y+1]-\sigma^2[y-1]}{\Delta y^2}\frac{(p[y+1]-p[y-1])}{2\Delta y}$
        $+\sigma^2[y]\frac{p[y+1]-2p[y]+p[x-1]}{\Delta x^2}$
    end for
  end for
  for each camera $j=1$ to M **do**
    for each grid point (x,y) **do**
      $b_{cam} \leftarrow [\mu_x(x,y,t)\ \mu_y(x,y,t)]^\top$
      // Update drift term: $\nabla \cdot (\mathbf{b}_{cam} p)$
      drift_cam_x $\leftarrow \frac{(p[x+1]-p[x-1])}{2\Delta x}\mu_x + \frac{(\mu_x[x+1]-\mu_x[x-1])}{2\Delta x}p[x]$
      drift_cam_y $\leftarrow \frac{(p[y+1]-p[y-1])}{2\Delta y}\mu_y + \frac{(\mu_y[y+1]-\mu_y[y-1])}{2\Delta y}p[y]$
    end for
  end for
  for each grid point (x,y) **do**
    $p_{new}[x,y] \leftarrow p[x,y] + \Delta t \cdot$ (drift_uav_x + drift_uav_y
      +diff_uav_x + diff_uav_y
      +drift_cam_x + drift_cam_y)
  end for
  $p \leftarrow p_{new}$ ▷ Set p for the next time step
end for
$N \leftarrow N_{new}$ ▷ Set N for increasing number of UAV

motion of transferring UAVs and cameras. In the UAV-driven segment, the number of UAVs is varied while consistent motion is maintained for two cameras, following Zigzag trajectories across different UAV quantities. The number of UAVs differs in each scenario, with 2, 5, 10, 15, and 20 values. For each distinct UAV count, FPE is solved to evaluate the expression (6). Regardless of the specific number of UAVs, the average time required for them to reach the boundary of the projection domain remains constant at 8 minutes—an indicator of the function's temporal behaviour. Due to this relatively short boundary-reaching time, the cameras do not complete their full trajectories. This is primarily attributed to an average velocity of 5 meters per second exhibited by the cameras, and in our case, each camera passes half of the trajectories. Despite this limitation, it suffices to assess the inter-dependencies between UAV and camera movements using regression analysis. To achieve this purpose, the same computational approach as previously described is employed to obtain the time-evolutionary

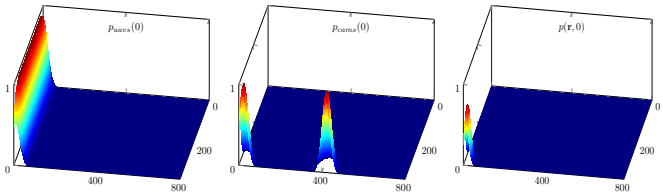

Fig. 4. The initial distributions of UAVs, cameras and joint, Left: $p_{uavs}(0)$, Center: $p_{cams}(0)$, Right: $p(\mathbf{r},0)$

numerical solutions of the FPE. Thus, each row delineates the

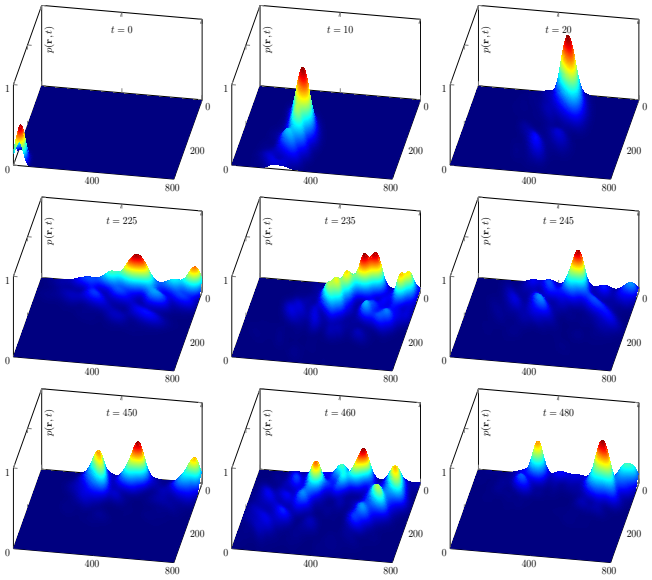

Fig. 5. The numerical solution of the FPE in different time evolution.

detection probabilities of each camera. The findings are succinctly presented in Table 1, wherein the initial column denotes the quantity of UAVs. This correlates with the time-dependent probabilities of two cameras positioned in the second and third columns. It is intuitive that as the number of UAVs escalates, the probabilities associated with both cameras must concurrently rise. At the onset of the starting time, it is expected that the first camera would exhibit a superior probability compared to the second camera. This anticipation arises from the proximity of the first camera's starting position to that of the UAVs, a phenomenon accurately captured in the computational analysis. Consequently, the cumulative duration spent by both cameras within the camera region amounts to 12 minutes for the first camera and 8 minutes for the second camera, considering their movement at a velocity of 5 meters per second. In conjunction with the temporal investigation, the assessment extends to quantifying the probabilities within each camera region, a factor contingent upon the speed of UAVs. A regression method is employed for consolidation to encapsulate all potential analyses comprehensively. Specifically, probabilities exceeding 0.5 are deemed reasonable and are visually denoted in green across all probability computations for both the first and second cameras. For UAV quantities ranging from 2 to 20, probabilities surpassing 0.5 for the first and second cameras range from 28 to 250 and 72 to 172, respectively. Subsequently, linear regression yields coefficients of 11.2 and 6.7,

Table 1. A UAV-driven capture probability estimation in two cameras

N	$P_1(t)$ of first camera	$P_2(t)$ of second camera
2	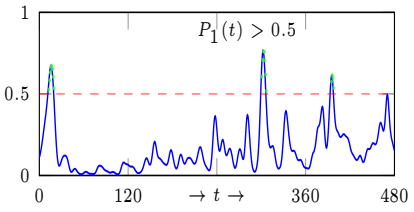	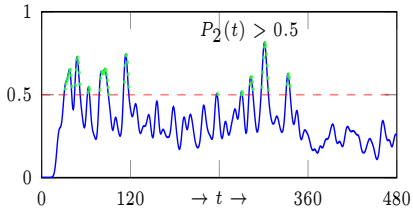
5	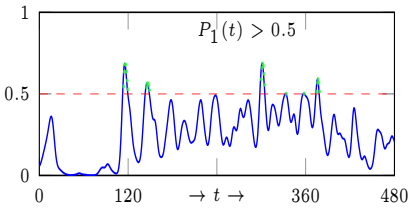	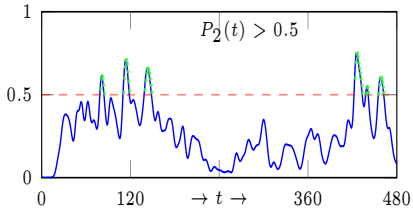
10	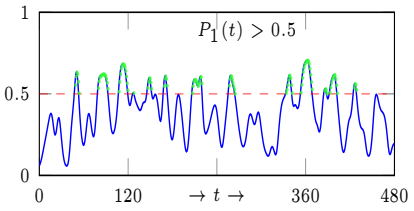	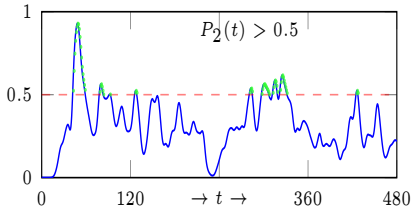
15	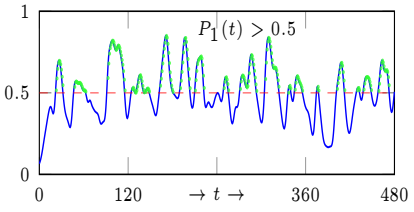	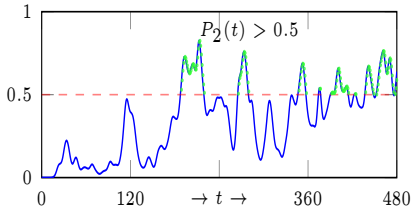
20	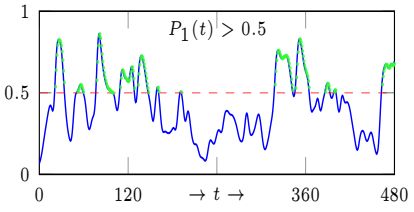	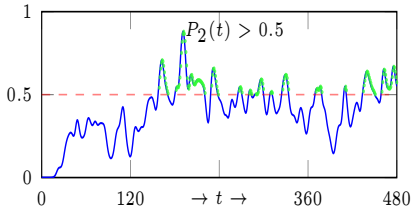
	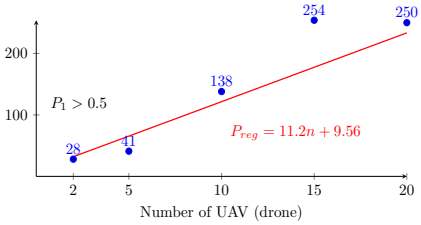	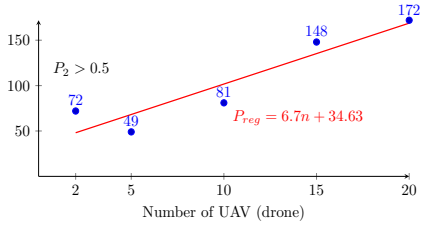

indicating that the first camera consistently maintains approximately twice the capture probability of the second camera region. A notable advantage of this computational approach is its consistent behaviour across multiple iterations, despite the random and varied generation of UAV paths in each run. However, the analysis lacks exploration into the effects of varying the speed of each UAV and camera, thus representing a potential avenue for future investigation.

3.2. Optimal Trajectory Control of Cameras for increasing UAVs capture through The Entropy Maximization

In the previous section, the reliability of the model was tested by changing the number of UAVs while keeping the trajectories of both cameras permanently set to Zigzag, ensuring coverage of the entire surveillance area. In this section, we extend the model to explore the optimal trajectories of both cameras for the best UAV capture and examine how to control them effectively. To quantify the system's uncertainty in this context, differential entropy, a widely used measure in fields such as control theory [26] and robotics [27], is employed.

We denote $\bar{p}(\mathbf{r},t)$ as the solution of (4) when the camera drift part is removed. Then the entropy at time t is calculated using the probability distribution $\bar{p}(\mathbf{r},t)$ as:

$$H(t) = -\int_{\Omega} \bar{p}(\mathbf{r},t)\log\bar{p}(\mathbf{r},t)d\mathbf{r},$$

which reflects the likelihood of UAVs being located at specific positions. This measure of uncertainty aligns with the broader concept of differential entropy, originally introduced by Shannon in the context of continuous probability distributions [28], which quantifies uncertainty in such systems and for more comprehensive examples are in [29].

A more dispersed and unpredictable UAV distribution results in higher entropy, reflecting greater uncertainty about their positions. Consequently, the camera must navigate the environment in a manner that maximizes the information gathered about UAVs, thereby reducing the uncertainty in their locations. This principle, rooted in information theory, was introduced in [30] and further elaborated using advanced techniques in [31]. Nevertheless, the camera must balance several objectives: maximizing entropy, minimizing energy or time expenditure, and maintaining continuous surveillance of its designated area. In this situation, the HJB equation is primarily used to determine the optimal trajectory, particularly in settings that involve both deterministic and uncertain environments. Some specific applications in optimal navigation can be found from [32,33], while solutions addressing fully stochastic and nonlinear dynamics with constraints have been explored in [34,35].

The control policy corresponds to the camera's movement, denoted as $\mathbf{u}_{cam}(t)$. The optimization of this control policy is achieved by defining a cost function that is minimized by solving the HJB equation:

$$\frac{\partial V(\mathbf{r},t)}{\partial t} + \min_{\mathbf{u}_{cam}(t)} \{-H(t) + \nabla_{\mathbf{r}} V(\mathbf{r},t)\cdot\mathbf{u}_{cam}(t)\} = 0,$$

in the equation $V(\mathbf{r},t)$ represents the value function, encapsulating the cost-to-go or reward-to-go, while $\mathbf{u}_{cam}(t)$ denotes the control input for the camera's drift. The value function reflects the best possible outcome starting from a specific position $\mathbf{r}$ and time t, extending to a designed future time horizon. In this way, $V(\mathbf{r},t)$ provides the optimal reward, directly related to maximizing entropy for a given camera position. Reflective boundary conditions are applied to the HJB equation to model the behavior of the camera at the edges of the surveillance domain, this means when the camera reaches the boundary, its control input $\mathbf{u}_{cam}(t)$ is reflected to maintain the same magnitude but with the direction adjusted based on the outward normal vector $\mathbf{n}$ at the boundary, this is expressed by the condition:

$$\mathbf{u}_{cam}(t)\cdot\mathbf{n} = -\mathbf{u}_{cam}(t)\cdot\mathbf{n}$$

The following Dirichlet boundary condition is introduced to incorporate operational constraints and strategic penalties, guiding the camera's trajectory to optimize its efficiency in capturing and engaging UAVs. This Dirichlet condition is not only reasonable in this context but also a deliberate choice to support an optimal control framework.

Thus, for the value function $V(\mathbf{r},t)$, we impose:

$$V(\mathbf{r},t) = V_{\text{exit}}(\mathbf{r}) \quad \text{for all } \mathbf{r}\in\partial\Omega$$

where $V_{\text{exit}}(\mathbf{r})$ is defined based on the high-probability regions for UAV encounters, formulated as a function of the distance from the point $\mathbf{r}$ to each target regions $\mathbf{r}_{\text{target}_i}$ with constants V_i, for more detail works on high probability region can be founded [36,37]:

$$V_{\text{exit}}(\mathbf{r}) = \sum_{i=1}^{2} V_i \exp\left(-\frac{\|\mathbf{r}-\mathbf{r}_{\text{target}_i}\|^2}{2\sigma_i^2}\right).$$

This formulation allows the value function to reflect a high likelihood in areas where UAV encounters are most probable, thereby guiding the camera efficiently.

The Dirichlet boundary condition ensures that $V(\mathbf{r},t)$ is directly determined on $\partial\Omega$, helping to implement operational constraints and avoid unintended influences outside this boundary. Furthermore, it aids in establishing uniqueness and convergence of the numerical solution [38,39], ensuring stability within the domain and mitigating boundary-based inconsistencies. With the Dirichlet condition applied, the value function aligns with operational constraints, supporting the objective of best UAV capture and engagement.

Hence, maximizing this entropy ensures that the camera focuses on areas characterized by uncertainty and dynamism, effectively tracking the UAVs' movements. To control the camera's trajectory for optimal information gathering, measured through entropy, we utilize the HJB equation, which is specifically designed for solving optimal control problems that require continuous decision making over time.

Resolving the HJB equation, we determine the optimal camera path $\mathbf{u}_{cam}(t)$ that ensures entropy $H(t)$ is maximized over time. The camera's motion is dynamically adjusted based on the current system state. The HJB equation guides how to modify the camera drift $\mathbf{u}_{cam}(t)$ at each time step, optimizing future entropy. This results in an adaptive control policy that ensures

Algorithm 2 Algorithm for Solving Optimal Camera Control using HJB Equation with Differential Entropy

Initialize parameters:
Define spatial grid: Δx, Δy and time step: Δt
Set final time T and initial value function $V(\mathbf{r},T) = V_{\text{exit}}(\mathbf{r})$
Define control set $\mathbf{u}_{cam}(t) \in \mathbb{U}_{cam}$ and apply boundary conditions:
  $V(\mathbf{r},t) = V_{\text{exit}}(\mathbf{r})$ for all $\mathbf{r} \in \partial\Omega$
Set initial condition $V(\mathbf{r},0)$ at each grid point
for each time step $n = N_t - 1$ to 0 with step size Δt **do**
  for each grid point (x,y) **do**
    $b_{cam} \leftarrow [\mu_x(x,y,t)\ \mu_y(x,y,t)]^\top$
    // Compute spatial gradient of V^n at (x,y)
    $\nabla V^n(x,y) \approx \begin{bmatrix} \frac{V(x+\Delta x,y)-V(x-\Delta x,y)}{2\Delta x} \\ \frac{V(x,y+\Delta y)-V(x,y-\Delta y)}{2\Delta y} \end{bmatrix}$
    // Solve Fokker-Planck equation to get $\bar{p}(\mathbf{r},t^n)$
    Update $\bar{p}(\mathbf{r},t^n)$ using FDM, with boundary condition $\frac{\partial \bar{p}}{\partial \mathbf{n}} = 0$
    // Compute entropy $H(t^n)$ using $\bar{p}(\mathbf{r},t^n)$
    $H(t^n) = -\int_\Omega \bar{p}(\mathbf{r},t^n)\log \bar{p}(\mathbf{r},t^n)\,d\mathbf{r}$
    // Find optimal control by minimizing over camera control
    $\mathbf{u}^n_{cam} = \arg\min_{\mathbf{u}_{cam}} \{-H(t^n) + \nabla_{\mathbf{r}} V^n \cdot \mathbf{u}_{cam}\}$
    // Update value function V^{n+1} using the HJB equation
    $V^{n+1}(x,y) \leftarrow V^n(x,y) + \Delta t \cdot (-(-H(t^n) + \nabla_{\mathbf{r}} V^n \cdot \mathbf{u}^n_{cam}))$
  end for
end for
Output: Optimal value function $V(\mathbf{r},0)$ and control trajectory $\{\mathbf{u}_{cam}(t)\}_{t=0}^{T}$

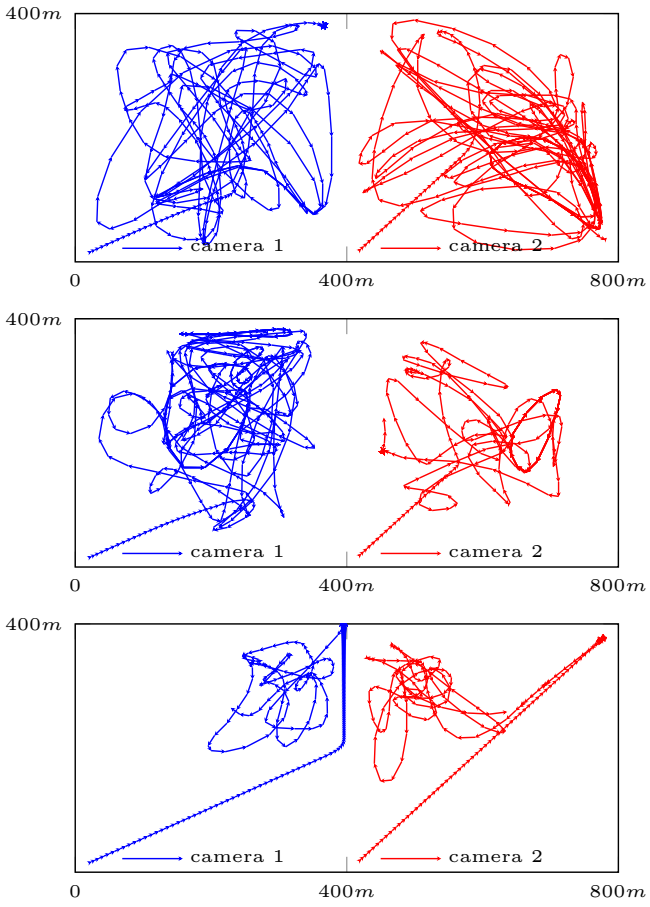

Fig. 6. Camera Drift Trajectories, Top: 10 UAVs, Center: 15 UAVs, Bottom: 20 UAVs.

that the camera moves consistently in a manner that effectively explores regions with high uncertainty, where UAVs exhibit unpredictable behavior.

For the numerical computation of the HJB equation, the domain is discretized in the same manner as implemented in the solution of the FPE. This ensures consistency in the grid and numerical methods applied across both equations.

The finite difference method, which proved effective for solving the FPE, is utilized here as well, and the pseudo-code expression to solve the HJB equation using FDM is illustrated in Algorithm 2. The initial condition $V(\mathbf{r},0)$ is defined as the squared Euclidean distance from the initial position of the camera $\mathbf{r}$ to the target point $\mathbf{r}_0$:

$$V(\mathbf{r},0) = \|\mathbf{r} - \mathbf{r}_0\|^2.$$

In this framework, the target position $\mathbf{r}_0$ is chosen as the average position of all UAVs, calculated as:

$$\mathbf{r}_0 = \frac{1}{N}\sum_{i=1}^{N} \mathbf{r}_{uav_i}(0)$$

where N is the total number of UAVs. This choice of target position allows the camera to optimize its trajectory toward the central area where UAVs are likely to be found, thus improving capture efficiency.

Considering two cameras, denoting their respective control inputs as u_{cam1} and u_{cam2}, these inputs correspond to the different trajectories that the cameras may follow while aiming to optimize UAV capture. The HJB equation, derived from the value function obtained in the FPE, guides the optimization of the cameras' paths based on the calculated probabilities of UAV encounters at each time step.

The interplay between the FPE and the HJB equation provides a structured framework for dynamically modeling camera trajectories. This framework is crucial to ensure that optimal controls adapt in real-time to probability distributions derived from FPE solutions, explores the relationship between the FPE and HJB equations, providing insight into how these equations can be solved in tandem to model controlled processes effectively [39]. By moving in the opposite direction of the gradient of the value function $V(\mathbf{r},t)$, the system naturally aligns with the gradient descent direction, which is essential for minimizing $V(\mathbf{r},t)$ and achieving optimality under the HJB framework, covers the role of gradient descent in optimal control and dynamic programming, including how the HJB equation is minimized through gradient-based approaches are [40].

This direction of gradient descent is central to satisfying the minimization condition inherent in the HJB equation, as it ensures that the camera's trajectories continuously adjust to reduce the cost associated with each state in real-time, and methodology for implementing gradient descent in the context of stochastic control problems can be found [41]. Consequently, this directional adjustment leads to control strategies that reflect real-time updates in probability densities, yielding a robust model for UAV encounter scenarios. This dynamic approach enhances capture and engagement strategies by allowing the camera to continuously move toward optimal observational positions while minimizing exposure and maximizing efficiency.

The results of camera drift trajectories are shown in Fig. 6. For 10 UAVs: The camera drift, denoted as $\mathbf{u}_{cam}(t)$, is substantial, leading to extensive movement of the camera across the domain. This high drift level suggests that when UAV density is lower, the camera control needs to respond more dynamically to monitor UAV positions effectively. This requires the camera to span larger distances and cover diverse directions, aligning with the need to capture more sparse information across the domain. For 15 UAVs: The camera drift decreases compared to the case with 10 UAVs. This reduced drift implies that a moderate increase in UAV density allows the camera control policy to stabilize. With more UAVs filling the space, the likelihood of UAVs covering critical regions increases, requiring less camera repositioning. This configuration reflects a more stable monitoring scenario, where the camera is less pressured to adjust drastically. For 20 UAVs: The camera drift is minimal, with the camera exhibiting shorter, less frequent movements.

As UAV density increases, the need for extensive camera repositioning is reduced, as the UAVs are likely to cover the domain more comprehensively. Here, the camera drift is nearly minimized, suggesting an optimal UAV density where the camera can remain relatively stationary while ensuring domain-wide surveillance.

The optimal trajectory lengths for two cameras were calculated as follows: $(10842m\ 15871m)$, $(8572m\ 7862m)$, and $(2514m\ 3231m)$ for 10, 15, and 20 UAVs, respectively. The computation time was approximately 8 minutes. The required angular speed varies with the distance, ranging from $3^o < \theta < 8^o$, where $\theta = v/f$; here, v represents the speed of the centroid within the camera's FOV, and f denotes the maximum distance of the camera's near FOV, Fig. 2, which is between $200m - 400m$ in our computations.

Commercial PTZ cameras can achieve rotational speeds up to 300° per second, a specification typical of professional-grade PTZ cameras used in security, broadcasting, and live event tracking. Therefore, the required tracking speed for this application falls well within the capabilities of most high-quality commercial PTZ cameras, which can comfortably handle these rotational requirements.

3.3. Cover Trajectory Maximizing Control for increasing UAVs capture through UAVs Encounter Probabilities

In this section, a comprehensive exploration is undertaken to unravel the intricate dynamics governing the interaction between UAVs and cameras, focusing specifically on the nuanced interdependence shaped by the camera's motion trajectory. The inquiry delves into the probability distribution spanning the spatial domain where the camera captures UAV movements within the surveillance area over the entire operational time frame. The evaluation of this probability is executed as a discerning metric, illuminating the complex nature of the correlation between UAVs and cameras.

Select different drift terms $\mathbf{b}^1_{cam_j}$, $\mathbf{b}^2_{cam_j}$,... that represent various camera behaviors such as constant drift, where the cameras move at a constant velocity, spatial dependent drift, where the cameras move faster near certain areas, and time-varying drift, where the cameras change their velocity depending on a time. For each drift term $\mathbf{b}^k_{cam_j}$, solve the FPE to obtain the corresponding probability density, then compute the cumulative probability:

$$P^k(\mathbf{r}) = \int_0^T p^k(\mathbf{r},t)dt \tag{7}$$

where $p^k(\mathbf{r},t)$ is the solution to FPE under the drift $\mathbf{b}^k_{cam_j}$, Then, define the optimal probability $P^*(\mathbf{r})$ as:

$$P^*(\mathbf{r}) = \min_k\{P^k(\mathbf{r})\}$$

This selection of $P^*(\mathbf{r})$ ensures that the drift term $\mathbf{b}^k_{cam_j}$ which minimizes the cumulative probability is chosen, representing the optimal camera behavior based on the minimized probability distribution.

To evaluate $P^k(\mathbf{r})$ the solution to Eq (4) needs to be derived for various camera trajectories. In this purpose, three distinct trajectories are focused: 1) zigzag, 2) spiral, and 3) random selected based on their differing predictability rates from the UAV perspective due to their distinct geometric features. Considering two adjacent areas for computational analysis, these three trajectories can produce three additional unique combinations. Visual representations of these trajectories are shown in Fig 7. The characteristic Zigzag pattern exhibits a regular and predictable structure owing to its repetitive sharp turns. In contrast, the Archimedean spiral displays a more continuous and gradually changing structure as it emanates from a central point, moving with a constant speed along the boundary of the surveillance area, which rotates at a constant angular velocity. In the case of the camera's motion, it initiates its trajectory in a random direction, subsequently bouncing off the boundary. Consequently, its unpredictability is notably higher compared to other motion patterns. The camera effectively covers the entire surveillance area following these three trajectories. The average time required for the camera to traverse the region along these paths is approximately 8 minutes. To estimate the camera-driven probability $P^k(\mathbf{r})$, the solution of the governing equation Eq. (4) is used concerning evolution time and its drift and diffusion terms. While different trajectories are assigned to the camera motion, fixed terms are applied for the UAV's drift and diffusion. Since the different trajectories are given for computing the drift term in solving Eq. (4), the simple differential is applied for considering the camera drift term. Then, the conventional trapezoidal rule is used to obtain the final probability.

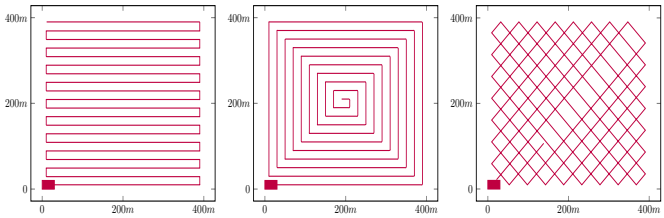

Fig. 7. Trajectories of the camera to cover the surveillance area, Left: zigzag, Center: spiral, Right: random-start.

Table 2. Two pair of coverage trajectory's UAV capture probability estimation.

Pair.Traj	$P(\mathbf{r})$	$P(\mathbf{r}) > 0.5$
$\mathcal{ZZ}$	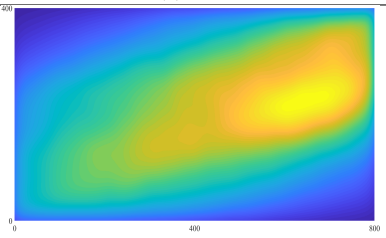	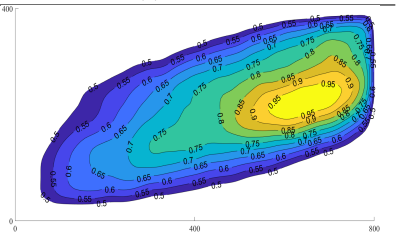
$\mathcal{SS}$	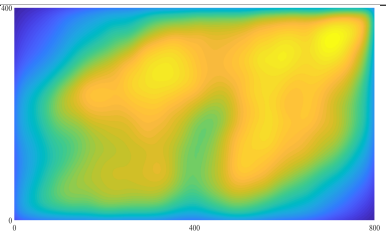	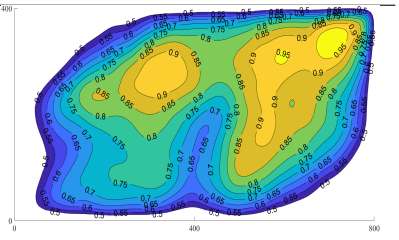
$\mathcal{RR}$	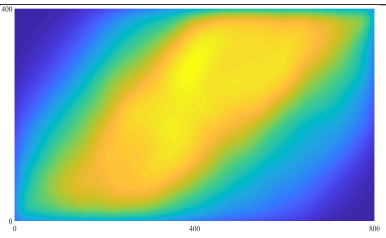	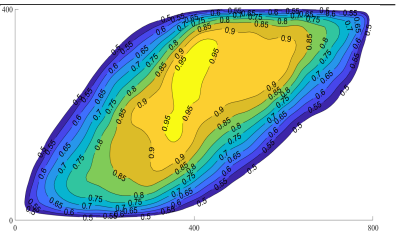
$\mathcal{ZS}$	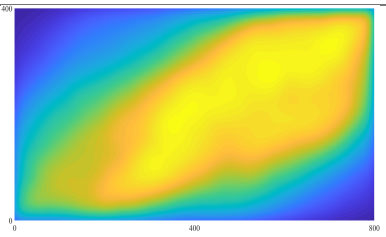	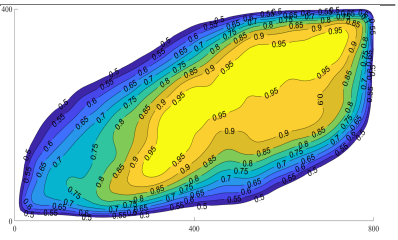
$\mathcal{SR}$	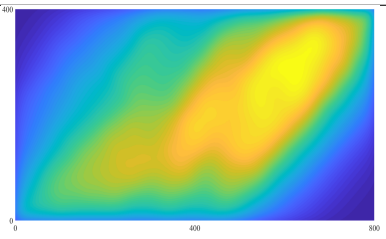	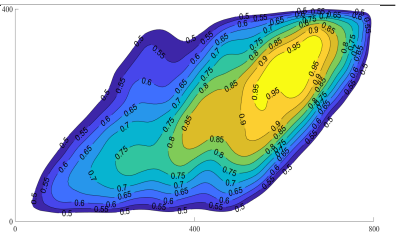
$\mathcal{RZ}$	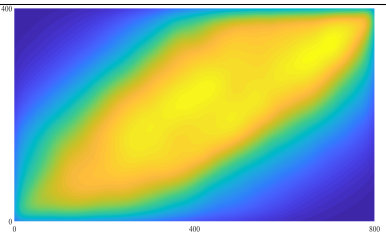	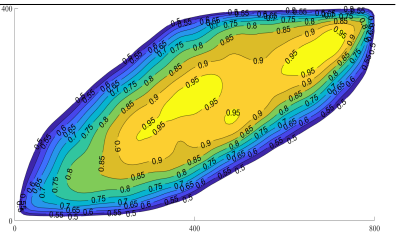

Additionally, denote Zigzag, Spiral, and Random trajectories as $\mathcal{Z}$, $\mathcal{S}$, and $\mathcal{R}$, then due to the commutative property in the divergence of Eq. (4), six different pairs of trajectories can be generated for two adjacent areas with two cameras, such as $\mathcal{ZZ}$, $\mathcal{SS}$, $\mathcal{RR}$, $\mathcal{ZS}$, $\mathcal{SR}$, and $\mathcal{RZ}$. For example, $\mathcal{SR}$ implies a pair of trajectories for two cameras: the first camera moves along the Spiral trajectory, the second camera moves the Random trajectory, and so on for other pairs. Table 2 compares the computational results of Eq. (7) concerning all pairs of cameras. An essential contribution of this study lies in its ability to identify the best pairs of cameras for many different purposes. Using 10 drones as UAVs with consistent tracks and speeds across all six considered scenarios, notable variations in results were observed, underscoring the impact of camera trajectories.

To elaborate, regions with a probability exceeding $P^k(\mathbf{r}) > 0.5$ were selected and are presented in column 3 of Table 2. Let $S(\text{pair trajectories})$ be the proportion area of the probability area at level c, The $S(P^k(\mathbf{r}) = c)$ represents the joint probability distribution area at the level c. To compute this area, the Shoelace method is applied and facilitates the computation of regions with probabilities greater than 0.5, and to ascertain the pair of camera trajectories with a joint probability distribution, the analysis evaluates the distribution area across three distinct levels, $c = 0.5$, 0.7 and 0.9. Based on the calculation results, the effectiveness of trajectory pairs for camera motion can be ranked as follows: 1. $\mathcal{ZS}$, 2. $\mathcal{SS}$, 3. $\mathcal{RR}$, 4. $\mathcal{SR}$, 5. $\mathcal{RZ}$, and 6. $\mathcal{ZZ}$. These experiments indicate that the most effective trajectory is $\mathcal{S}$-type.

The Python plotting tool, MATLAB, and LaTeX pgfplot packages were used throughout the paper's results and visualizations.

4. CONCLUSION

This research has successfully modeled the joint distribution of interaction between UAVs and surveillance camera movements using a fundamental differential equation.

The model incorporates UAV movement, tailored to accommodate the unique flight patterns of UAVs, and its reliability test was successful. In particular, varying the number of UAVs and the capture ratio of each camera's slope resulted in values of 11.2 and 6.7, with intercepts of 9.56 and 34.63, respectively. The first camera is more sensitive than the second, which implies that the UAV's starting position is closer to the first camera. The second camera's higher intercept indicates a larger field for capture.

The two scenarios were carefully evaluated for simulation compatibility with computational and real-world constraints to determine the optimal camera path. An entropy-maximizing method was successfully applied, yielding the optimal camera path based on the number of UAVs and effectively bridging computational results with real-world interpretation. For example, the ratio of the two camera paths' lengths in relation to UAV counts were 1.26 2.01; 3.40 2.43; and 4.31 4.91 for 10/15, 15/20, and 10/20 UAVs, respectively. Given the same surveillance area and UAV runtime, these results allow us to estimate the speed requirements for each camera. Moreover, this algorithm demonstrates strong potential for application in control systems.

Additionally, a probability-based method was used to identify optimal coverage paths for two pairs of cameras, resulting in six different trajectory configurations across two adjacent areas. The paths denoted as $\mathcal{ZS}$ (a combination of zigzag and spiral) and $\mathcal{SS}$ (a combination of spiral and spiral) showed significantly better performance, achieving coverage efficiency up to 1.29-3 times higher than other trajectory pairs.

This indicates that utilizing these models could enhance the probability of success. Therefore, our future work will focus on real-time detection and world-coordinate optimization for anti-UAV systems, building upon the methods proposed in this study.

ACKNOWLEDGEMENTS

This research was supported by the Institute of Civil-Military Technology Cooperation, funded by the Defense Acquisition Program Administration and the Ministry of Trade, Industry, and Energy of the Korean government under Grant 22-SN-EC-16.

REFERENCES

[1] P. Ekka, "A Review Paper on Unmanned Aerial Vehicle (U.A.V.)," *Int. Jour. of Eng. Res. and Tech*, vol. 5, no. 23, pp. 1-3, 2017, doi: 10.17577/IJERTCONV5IS23008.

[2] S. A. H. Mohsan, N. Q. H. Othman, Y. Li, M. H. Alsharif, and M. A. Khan, "Unmanned aerial vehicles (UAVs): practical aspects, applications, open challenges, security issues, and future trends," *Intel. Serv. Rob.*, vol. 16, pp. 109-137, 2023, doi: 10.1007/s11370-022-00452-4.

[3] P. Szywalski and A. Waindok, "A decentralized radio network for small groups of unmanned aerial vehicles," *Bull. Pol. Acad. Sci. Tech. Sci.*, vol. 72, no. 1, p. e147922, 2024, doi: 10.24425/bpasts.2023.147922.

[4] A. Parrek, V. Singh, and A. Jain, "Detection Algorithms for Detecting Drones/UAVs," *Darpan Int. Res. Analysis*, vol. 12, no. 3, pp. 340-351, 2024, doi: 10.36676/dira.v12.i3.93.

[5] L. Bi, Z.-X. Xu, and L. Yang, "Low-cost UAV detection via WiFi traffic analysis and machine learning," *Sci Rep* vol. 13, 20892, 2023, doi: 10.1038/s41598-023-47453-6.

[6] J. Łukasiewicz and T. A. Kobaszyńska, "Proposed method for building an anti-drone system for the protection of facilities important for state security," *Sec and Def Quart*, vol. 39, no. 3, pp. 88–107, 2022, doi: 10.35467/sdq/149268.

[7] X. Zhang and K. Kusrini, "Autonomous long-range drone detection system for critical infrastructure safety," *Mult. Tools and App.*, vol. 80, pp. 23723–23743, 2021, doi: 10.1007/s11042-020-10231-x.

[8] R. A. Zitar, M. Al-Betar, M. Ryalat, and S. Kassaymeh, "A review of UAV Visual Detection and Tracking Meth-

ods," *arXiv e-Print Archive*, 2023, doi: 10.48550/arXiv.2306.05089.

[9] J. Zhao, J. Zhang, D. Li, and D. Wang, "Vision-Based Anti-UAV Detection and Tracking," *IEEE Trans. on Intel. Trans. Sys*, vol. 23, no. 12, pp. 25323-25333, 2022, doi: 10.1109/TITS.2022.3177627.

[10] N. Al-lQubaydhi, A. Alenezi, T. Alanazi, A. Senyor, N. Alanezi, B. Alotaibi, M. Alotaibi, A. Razaque, and S. Hariri, "Deep learning for unmanned aerial vehicles detection: A review," *Com. Sci. Rev*, vol. 51, p. 100614, 2024, doi: 10.1016/j.cosrev.2023.100614.

[11] Y. I. Kim, Y. G. Min, P. S. Hee, J. Wun-Cheol, S. Soonyong, and H. Tae–Wook, "The analysis of image acquisition method for Anti-UAV surveillance using cameras image," in *Proceedings of International Conference on Information and Communication Technology Convergence (ICTC)*, Jeju, South Korea, 2020, pp. 545-549, doi: 10.1109/ICTC49870.2020.9289164.

[12] A. S. Olagoke, H. Ibrahim, and S. S. Teoh, "Literature Survey on Multi-Camera System and Its Application," *IEEE Access*, vol. 8, pp. 172892-172922, 2020, doi: 10.1109/ACCESS.2020.3024568.

[13] T. I. Amosa, P. Sebastia, L. I. Izhar, O. Ibrahim, L. S. Ayinla, A. A. Bahashwan, A. Bala, and Y. A. Samaila, "Multi-camera multi-object tracking: A review of current trends and future advances," *Neurocom.*, vol. 552, Paper 126558, 32 pages, 2023, doi: 10.1016/j.neucom.2023.126558.

[14] P. Natarajan, P. K. Atrey, and M. Kankanhalli, "Multi-Camera Coordination and Control in Surveillance Systems: A Survey," *ACM Trans. on Mult. Comp., Comm, and App*., vol. 11, no. 4, pp. 1-30, 2015, doi: 10.1145/2710128.

[15] Y. I. Kim, Y. G. Min, P. S. Hee, J. Wun-Cheol, S. Soonyong, and H. Tae–Wook, "The analysis of UAV detection performance using rotating cameras," in *Proceedings of International Conference on Information and Communication Technology Convergence (ICTC)*, Jeju, South Korea, 2021, pp. 1262-1265, doi: 10.1109/ICTC52510.2021.9621076.

[16] P. J. Smith, I. Singh, P. A. Dmochowski, J. P. Coon, and R. Green, "Flexible Mobility Models Using Stochastic Differential Equations," *IEEE Trans. on Veh. Tech*., vol. 71, no. 4, pp. 4312-4321, 2022, doi: 10.1109/TVT.2022.3146407.

[17] B. Oksendal, "Stochastic Differential Equations" In: *Universitext book series - Stochastic Differential Equations: An Introduction with Applications*, Berlin, Heidelberg: Springer, 2003, pp. 65-84, doi: 10.1007/978-3-642-14394-6_5.

[18] P. Kumari, N. Nandyala, A. K. S. Teja, N. Goel, and M. Saini, "Dynamic Scheduling of an Autonomous PTZ Camera for Effective Surveillance," in *Proceedings of the IEEE 17th International Conference on Mobile Ad Hoc and Sensor Systems (MASS)*, 2020, pp. 437-445, doi: 10.1109/MASS50613.2020.00060.

[19] E. Galceran and M. Carreras, "A survey on coverage path planning for robotics," *Robotics and Autonomous Systems*, vol. 61, no. 12, pp. 1258–1276, 2013, doi: 10.1016/j.robot.2013.09.004.

[20] M. Annunziato and A. Borzì, "A Fokker–Planck control framework for stochastic systems," *EMS Surveys in Mathematical Sciences*, vol. 5, no.1/2, pp. 65–98, 2018, doi: 10.4171/EMSS/27.

[21] H. Risken, "The Fokker-Planck Equation," in *Springer Series in Synergetics - The Fokker-Planck Equation: Method of Solution and Applications*, vol. 18, Berlin, Heidelberg: Springer, 1989, pp. 63-95, doi: 10.1007/978-3-642-61544-3.

[22] L. Pichler, A. Masud, and L. A. Bergman, "Numerical Solution of the Fokker–Planck Equation by Finite Difference and Finite Element Methods—A Comparative Study," in *Computational Methods in Applied Sciences Book Series - Comp. Meth. in Stoch. Dyn.*, M. Papadrakakis, G. Stefanou, and V. Papadopoulos, Eds. vol. 26, Dordrecht: Springer, 2013, pp. 69-85, doi: 10.1007/978-94-007-5134-7_5.

[23] C. R. Qi, W. Liu, C. Wu, H. Su, and L. J. Guibas, "Frustum PointNets for 3D Object Detection from RGB-D Data," in *Proceedings of IEEE/CVF Conference on Computer Vision and Pattern Recognition (CVPR)*, Salt Lake City, UT, USA, 2018, pp. 918-927, doi: 10.1109/CVPR.2018.00102.

[24] S. Polidoro, "Uniqueness and representation theorems for solutions of Kolmogorov-Fokker-Planck equations," *Rendiconti di Matematica e delle sue Applicazioni. Serie VII*, vol. 15, pp. 535-560, 1995.

[25] V. Bogachev, G. Da Prato, and M. Röckner, "Existence and uniqueness of solutions for Fokker–Planck equations on Hilbert spaces" *J. Evol. Equ.*, Springer, vol. 10, pp. 487–509, 2010, doi: 10.1007/s00028-010-0058-y.

[26] G. N. Saridis, "Entropy formulation of optimal and adaptive control," *IEEE Trans. on Auto. Cont*, vol. 33, no. 8, pp. 713-721, 1988, doi: 10.1109/9.1287.

[27] H. Shen, Q. Wang, and Y. Yi, "Event-Triggered Tracking Control for Adaptive Anti-Disturbance Problem in Systems with Multiple Constraints and Unknown Disturbances," *Entropy*, vol. 25, no. 1, p. 43, 2023, doi: 10.3390/e25010043.

[28] C. E. Shannon, "A mathematical theory of communication," *The Bell. Sys. Tech. Jour.*, vol. 27, no. 3, pp. 379-423, 1948, doi: 10.1002/j.1538-7305.1948.tb01338.x.

[29] J. V. Michalowicz, J. M. Nichols, and F. Bucholtz, *Handbook of Differential Entropy, 1st ed.*, Chapman and Hall/CRC, 2013, doi: 10.1201/b15991.

[30] E. T. Jaynes, *Information theory and statistical mechanics*, ser. American Physical Society, 1957, vol. 106, pp. 620-630, doi: 10.1103/PhysRev.106.620.

[31] D. E. Holmes, *Jaynes and the Principle of Maximum Entropy*. Santa Fe Institute Press, 2017, doi: 10.37911/9781947864528.14.

[32] C. Parkinson, D. Arnold, A. L. Bertozzi, Y. T. Chow, and S. Osher, “Optimal human navigation in steep terrain:

a Hamilton Jacobi-Bellman approach," *Comm in Math Sci*, vol. 17, no. 1, pp. 227–242, 2019, doi: 10.48550/arXiv.1805.04973

[33] C. Parkinson, D. Arnold, A. Bertozzi, and S. Osher, "A model for optimal human navigation with stochastic effects," *SIAM Journal on Applied Mathematics*, vol. 80, no. 4, pp. 1862–1881, 2020, doi: 10.1137/19M1296537.

[34] J. Qui, "Viscosity solutions of Hamilton-Jacobi-Bellman equations," *SIAM Journal on Control and Optimization*, vol. 56, no. 5, pp. 3708-3730, 2018, doi: 10.1137/17M1148232.

[35] J. Weston, D. Tolić, and I. "Palunko, Application of Hamilton–Jacobi–Bellman Equation/Pontryagin's Principle for Constrained Optimal Control," *J Optim Theory Appl*, vol. 200, pp. 437–462, 2024, doi: 10.1007/s10957-023-02364-4.

[36] M. S. Arulampalam, S. Maskell, N. Gordon, and T. Clapp, "A tutorial on particle filters for online nonlinear/non-Gaussian Bayesian tracking," *IEEE Trans. on Sig Proc*, vol. 50, no. 2, pp. 174-188, 2002, doi: 10.1109/78.978374.

[37] S. Thrun, W. Burgard, and D. Fox, *Probabilistic Robotics*, MIT Press, 2005. [Online]. Available: https://books.google.co.kr/books?id=2Zn6AQAAQBAJ.

[38] M. Bardi and I. Capuzzo-Dolcetta, *Optimal Control and Viscosity Solutions of Hamilton-Jacobi-Bellman Equations*, Birkhäuser, 1997, doi: 10.1007/978-0-8176-4755-1.

[39] W. H. Fleming and H. Soner, *Controlled Markov Processes and Viscosity Solutions*, Springer, 2006, doi: 10.1007/0-387-31071-1.

[40] D. P. Bertsekas, "Approximate Dynamic Programming," in *MIT Handbook - Dynamic Programming and Optimal Control, 3rd Ed.*, Massachusetts Institute of Technology, 2011, [Online]. Available: https://web.mit.edu/dimitrib/www/dpchapter.pdf.

[41] H. J. Kushner and P. Dupuis, "Construction of the approximating Markov Chain," in *Applications of Mathematics - Numerical Methods for Stochastic Control Problems in Continuous Time*, vol. 24, New York, NY: Springer, 2001, pp. 89–151, doi: 10.1007/978-1-4613-0007-6.